Earth and Space Science

METHOD

10.1029/2024EA003675

# MAGPRIME: An Open-Source Library for Benchmarking and Developing Interference Removal Algorithms for Spaceborne Magnetometers

**Alex Paul Hoffmann[1], Mark B. Moldwin[1], Shun Imajo[2], Matthew G. Finley[3], and Arie Sheinker[4]**

[1]Climate and Space Sciences and Engineering, University of Michigan, Ann Arbor, MI, USA, [2]Data Analysis Center for Geomagnetism and Space Magnetism, Graduate School of Science, Kyoto University, Kyoto, Japan, [3]NASA Goddard Space Flight Center, Greenbelt, MD, USA, [4]Soreq Nuclear Research Center, Yavne, Israel

**Abstract** Magnetometers are essential instruments in space physics, but their measurements are often contaminated by various external interference sources. In this work, we present a comprehensive review of existing magnetometer interference removal methods and introduce MAGPRIME (MAGnetic signal PRocessing, Interference Mitigation, and Enhancement), an open-source Python library featuring a collection of state-of-the-art interference removal algorithms. MAGPRIME streamlines the process of interference removal in magnetic field data by providing researchers with an integrated, easy-to-use platform. We detail the design, structure, and functionality of the library, as well as its potential to facilitate future research by enabling rapid testing and customization of interference removal methods. Using the MAGPRIME Library, we present two Monte Carlo benchmark results to compare the efficacy of interference removal algorithms in different magnetometer configurations. In Benchmark A, the Underdetermined Blind Source Separation (UBSS) and traditional gradiometry algorithms surpass the uncleaned boom-mounted magnetometers, achieving improved correlation and reducing median error in each simulation. Benchmark B tests the efficacy of the suite of MAGPRIME algorithms in a boomless magnetometer configuration. In this configuration, the UBSS algorithm proves to significantly reduce median error, along with improvements in median correlation and signal to noise ratio. This study highlights MAGPRIME's potential in enhancing magnetic field measurement accuracy in various spacecraft designs, from traditional gradiometry setups to compact, cost-effective alternatives like bus-mounted CubeSat magnetometers, thus establishing it as a valuable tool for researchers and engineers in space exploration and magnetism studies.

**Plain Language Summary** Magnetometers, tools used to measure magnetic fields, are crucial for space exploration but often face interference from a spacecraft's own systems. This can distort measurements, making it hard to get accurate data. In order to address this, we introduce MAGPRIME, an open-source software that helps clean up these magnetic field measurements. It is user-friendly and integrates various techniques to reduce interference in the data. We tested MAGPRIME in two scenarios: one with magnetometers on a long mechanical arm or boom, and another without the boom. The results from these cases show that the use of MAGPRIME can make it easier and cheaper to get reliable magnetic field data, especially for smaller satellites like CubeSats.

**Key Points:**

- MAGPRIME is an open-source Python library with advanced interference removal algorithms for magnetic field measurements in space missions
- The MAGPRIME library is designed to be a community-driven platform for magnetometer signal processing algorithms
- Monte Carlo simulation results show UBSS achieves significant interference reduction in both boom and bus-mounted magnetometer setups

**Correspondence to:**

A. P. Hoffmann,
aphoff@umich.edu

**Citation:**

Hoffmann, A. P., Moldwin, M. B., Imajo, S., Finley, M. G., & Sheinker, A. (2024). MAGPRIME: An open-source library for benchmarking and developing interference removal algorithms for spaceborne magnetometers. *Earth and Space Science*, *11*, e2024EA003675. https://doi.org/10.1029/2024EA003675

Received 1 APR 2024
Accepted 1 JUN 2024

**Author Contributions:**

**Conceptualization:** Alex Paul Hoffmann
**Data curation:** Alex Paul Hoffmann
**Formal analysis:** Alex Paul Hoffmann
**Funding acquisition:** Mark B. Moldwin
**Investigation:** Alex Paul Hoffmann
**Methodology:** Alex Paul Hoffmann, Shun Imajo, Matthew G. Finley, Arie Sheinker
**Project administration:** Mark B. Moldwin
**Resources:** Mark B. Moldwin
**Software:** Alex Paul Hoffmann
**Supervision:** Mark B. Moldwin
**Validation:** Alex Paul Hoffmann
**Visualization:** Alex Paul Hoffmann
**Writing – original draft:** Alex Paul Hoffmann



## 1. Introduction

Space exploration missions often require magnetic field measurements, but these measurements can be distorted by stray magnetic fields generated by spacecraft electrical systems. This interference can come from various subsystems, such as reaction wheels, magnetorquers, propulsion systems, and others. Interference sources typically include permanent magnetization (hard iron), induced magnetization (soft iron), eddy currents, and current loops (stray fields). One method to reduce stray magnetic field interference is to place the magnetometer on a long mechanical boom, so that the stray magnetic fields diminish with distance. However, this is not always effective, as many spacecraft still experience interference from different source even with a boom. For example, the InSight rover has a single magnetometer on a short boom and observes high-frequency interference associated with solar panel currents (Johnson et al., 2020). The DMSP F15 satellite has a 5 m boom and struggles with spacecraft interference (Kilcommons et al., 2017). The GOES-17 spacecraft has a 6 m boom but observes interference from arcjet activity and reaction wheels (Califf et al., 2020; Loto'aniu et al., 2019). Stray magnetic

**Writing – review & editing:** Mark B. Moldwin, Shun Imajo, Matthew G. Finley, Arie Sheinker

fields have been challenging spacecraft magnetometers since the first spaceflight magnetometer was launched in 1958 (Dolginov et al., 1961).

To mitigate the effects of stray magnetic field interference, two main methods have been developed over the years. The first method is magnetic cleanliness, which aims to minimize the generation of stray magnetic fields by modifying the electrical and mechanical design of the spacecraft (Lassakeur et al., 2020; Ludlam et al., 2009; Nikolopoulos et al., 2020). This can be done by using non-magnetic materials, running wires in twisted-pairs, minimizing current loops, and shielding high power instruments. However, magnetic cleanliness is not always feasible, especially for low cost or mass produced spacecraft such as CubeSats. The second method is gradiometry, which uses two or more magnetometers to estimate and remove the interference signals (Jo et al., 2023; Kivelson et al., 2023; Lee et al., 2023). Ness et al. (1971) proposed a gradiometry algorithm that assumes the spacecraft magnetic field as a dipole and removes it using the gradient between two magnetometers placed collinearly on a boom. This method requires a long enough boom for the dipole assumption to be valid, but can use a shorter boom if the spacecraft's magnetic field is well-characterized.

Several recent gradiometry algorithms have been developed to deal with more complex interference scenarios. Sheinker and Moldwin (2016) developed an adaptive algorithm (denoted Sheinker) that identifies the gain of the stray magnetic field between magnetometers through a machine learning technique, and subtracts the estimated field using that gain. This algorithm can handle both static and dynamic interference sources, and does not require prior knowledge of the field characteristics. Carter et al. (2016) developed an algorithm that switches between gradiometry or averaging depending on the ratio of stray magnetic field interference to intrinsic magnetometer noise. Constantinescu et al. (2020) developed the Principal Component Gradiometry (PiCoG) algorithm, which transforms the dual-magnetometer measurements into a new coordinate system derived from principle component analysis, and performs gradiometry along the direction of maximum-variance. This algorithm can effectively suppress interference, and can be applied to any number of magnetometers. Ream et al. (2021) developed a gradiometry algorithm (denoted Ream) that detects stray magnetic field signals by differencing the magnetometer measurements in the time-domain and suppressing them in the frequency-domain.

Without the use of a boom, simplifying approximations can not be made about the structure of the spacecraft's magnetic field, so removing the stray magnetic field interference becomes much more challenging. Several advanced methods have been proposed to address this issue, such as Independent Component Analysis (ICA), Multichannel Singular Spectrum Analysis (M-SSA), Underdetermined Blind Source Separation (UBSS), and Wavelet-based Adaptive Interference Cancellation for Underdetermined Platforms (WAIC-UP). These methods can separate interference signals from the natural magnetic field signal without prior knowledge of the interference characteristics, and can work with more than two magnetometers. ICA is a technique that separates interference signals based on their statistical independence, but it can only handle a limited number of interference sources (Imajo et al., 2021). M-SSA is a technique that decomposes the signal components in the time domain, but it requires careful selection of the components to reconstruct the natural magnetic field signal (Finley et al., 2023). UBSS is a novel technique that exploits the multi-magnetometer configuration to identify interference signals using cluster analysis and applies compressive sensing to separate the interference from the ambient magnetic field, however it is computationally complex and requires many data-dependent parameters to be tuned (Hoffmann & Moldwin, 2022). The WAIC-UP algorithm exploits the distinct spectral properties of various interference signals to separate them from the ambient magnetic field in the wavelet domain (Hoffmann & Moldwin, 2023). WAIC-UP is efficient at cleaning high-frequency interference and orders of magnitude faster than UBSS, but it cannot clean lower frequency interference due to the limitations of the wavelet transform. These algorithms are effective at cleaning bus-mounted magnetometer measurements as they can work with multiple magnetometers with minimal assumptions about the nature of the stray magnetic fields. The aforementioned algorithms correct magnetometer measurement errors caused by external interference and are distinct from calibration techniques, which adjust for internal errors in gain, bias, and axis orthogonality (Foster & Elkaim, 2008; Springmann & Cutler, 2012; Vasconcelos et al., 2011).

In this work, we introduce MAGPRIME, an open-source tool for magnetometer signal processing. MAGPRIME is a Python library that offers a variety of interference removal algorithms for magnetometer data. It aims to foster community-driven development of magnetometer interference removal applications and to support future spacecraft design. Additionally, this library enables the creation of simulations of distributed interference sources and magnetometers in various spacecraft layouts. We use the MAGPRIME library to compare several

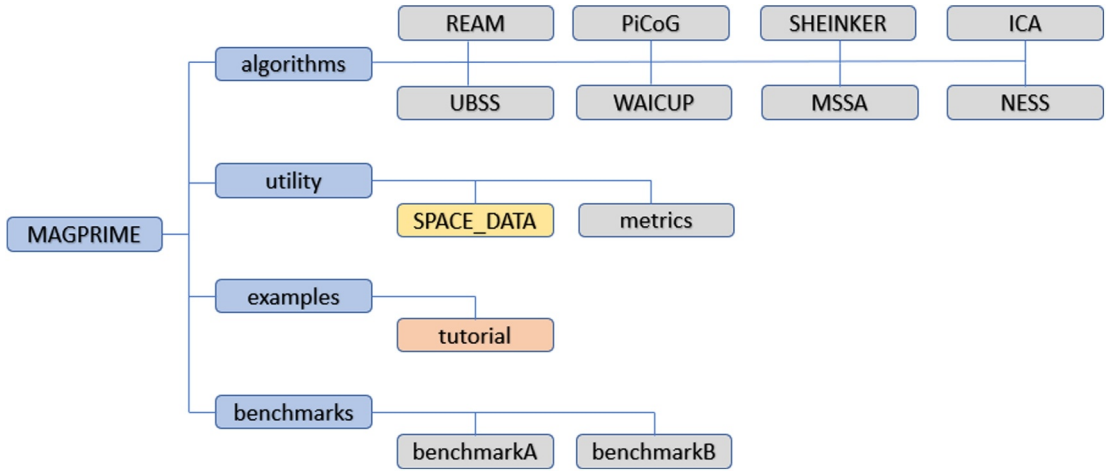


**Figure 1.** Overview of the functionality of the MAGPRIME Python library. Folders are shown in blue, files are shown in gray, data are shown in yellow, and Jupyter notebooks are in light orange.

interference removal algorithms with Monte Carlo simulations. We consider two scenarios for the simulations. The first is the standard gradiometry case, where two magnetometers are mounted on a short boom. The second case is where three magnetometers are mounted on the spacecraft bus. The boomless configuration is a low cost alternative to typical gradiometry with a mechanical boom, but experiences significantly more stray magnetic field interference. We evaluate the performance of the MAGPRIME interference removal algorithms on highly broadband and complex magnetic field interference. MAGPRIME enhances space physics and spacecraft design research by offering advanced algorithms for stray magnetic field removal. Its ability to provide accurate magnetic field measurements is crucial for the success of in situ space science missions. In this work, we showcase MAGPRIME's effectiveness and highlight its potential for broad adoption in future space explorations.

## 2. Software Description

MAGPRIME is a Python package that offers a comprehensive set of interference removal algorithms for space-based magnetic field measurements. It is an open-source and community-based project that aims to enable the development and evaluation of new and existing methods for improving the quality and reliability of magnetometer data. The package is hosted on GitHub under the CC BY-NC 4.0 license and invites contributions from researchers in space sciences and engineering. The open-source nature of the project not only ensures collaborative development and transparency, but also aligns with the spirit of the NASA's Open Science Initiative (Gustetic et al., 2015).

The package provides the following functionality:

1. A collection of interference removal algorithms, such as WAIC-UP, UBSS, M-SSA, and others.
2. Example scripts and Jupyter notebooks to demonstrate the usage of the library and show the results of applying different algorithms to real and synthetic data sets.
3. Two benchmarks to evaluate the efficacy of each algorithm on different magnetometer configurations.

Figure 1 illustrates the structure of the Python package. The package consists of four main modules: algorithms, utilities, examples, and benchmarks. Each module contains files that implement the corresponding functionality. The package offers a user-friendly interface that allows users to easily import and use the algorithms on their data.

The package can be installed using pip or by cloning the repository and running setup.py or pip install. The package requires Python 3.9 or higher and depends on several external packages, such as numpy, scipy, matplotlib, etc. The package also includes detailed usage instructions and examples in the README file and the examples folder.

The following code snippet demonstrates how to import the 'magprime' library and use its interference removal algorithms on spacecraft magnetometer data. Some algorithms necessitate detrending of the data, for which

purpose each algorithm is equipped with specific parameters like *uf* and *detrend*. The *uf* parameter specifies the number of data points to be used in a uniform filter, while the *detrend* parameter is a boolean that indicates whether data detrending should be done or not. Here is an example of interference removal using the WAIC-UP algorithm:

**Listing** 1. Interference Removal Example Using the WAIC-UP Algorithm

```
from magprime.algorithms import WAICUP
from magprime import utility

"Load example data from Michibiki-1 Satelltie"
B = utility.load_example_data() # shape = (n_sensors, n_axes, n_samples)

"Detrend the data"
WAICUP.uf = 360   # n_samples to use in uniform filter
WAICUP.detrend = True

"Algorithm Parameters"
WAICUP.fs = 1     # Sample rate
WAICUP.dj = 1/12  # Wavelet Spacing

"Clean the data and store it in B_waicup"
B_waicup = WAICUP.clean(B, triaxial = True)
```

Each algorithm also has specific parameters that are unique to its functionality and can be defined by the user. For example, the WAIC-UP algorithm has the parameter, *WAICUP.dj*, that controls the resolution of its wavelet transformation. These algorithm-specific parameters are explained in detail in the tutorial notebook of the "magprime" library. They can be accessed by using the help function, for example, *help*(*WAICUP*).

Moreover, each algorithm has a clean() function that takes the noisy magnetic field data as input and returns the cleaned data as output. This is the function that intakes the noisy magnetometer data from multiple magnetometers and returns an individual, cleaned triaxial signal. Some algorithms are developed to work on only triaxial data, while others can clean both triaxial or single axis data. The *triaxial* argument is used to specify whether the data are single axis or triaxial.

### 2.1. Potential Applications

The "magprime" library is designed to be both a research tool and a utility for magnetic interference removal from past and future satellite mission data sets. The library serves three key purposes in the field of space magnetism research:

1. It is a hub for the development of magnetic interference removal algorithms, providing several benchmarks that standardizes their comparison. This ensures that researchers can reliably select the most effective algorithm for specific interference conditions in magnetometer data.
2. It can be adapted for cleaning operational spacecraft magnetometer data, thereby enhancing the precision of magnetic field measurements collected during space missions.
3. It aids in the design phase of spacecraft by providing simulations to determine optimal magnetometer placement. For spacecraft that use booms, MAGPRIME can determine the minimum length of the boom to minimize the spacecraft's magnetic interference.

The "magprime" library is an open-source project that encourages enhancement through its community-driven approach. It welcomes new algorithms and updates from contributors. By refining the quality of space-based

magnetic field measurements, the library aims to support studying investigations of space magnetism throughout the heliosphere.

## 3. Methodology

Since the first spacecraft magnetometer flew in 1958, many interference removal algorithms have been created. These algorithms vary in their approach to different types of interference from DC offsets to higher frequency interference from subsystems such as reaction wheels. In the first part of this section, we review the methodology of several interference removal algorithms that are included in MAGPRIME. These algorithms are recreated from their original papers and are undergoing continuous development to improve their functionality. In the second part of this section, we describe the methods used to create the Monte Carlo simulations used to benchmark the algorithms. These simulations include a variety of simulated and real magnetometer interference.

### 3.1. Algorithms

#### 3.1.1. Gradiometry

Ness et al. (1971) proposed the seminal algorithm for removing the magnetic interference caused by the spacecraft. The technique relies on two magnetometers mounted collinearly on a boom to measure the observed magnetic field at different distances from the spacecraft. The algorithm assumes that the spacecraft's magnetic field can be approximated by a single effective dipole field, and estimates its presence at each sensor. The coupling matrix, $\alpha$, captures the relationship between the spacecraft's field and the measurements at the two sensors. The algorithm then recovers the ambient magnetic field, $B_{amb}^{est}$, by using the following equation:

$$B_{amb}^{est} = \frac{B_{obs}(r_2) - \alpha B_{obs}(r_1)}{1 - \alpha} \tag{1}$$

In this system, $B_{obs}(r_2)$ and $B_{obs}(r_2)$ are the observed fields at the midpoint and the end of the boom, respectively. This gradiometry algorithm necessitates an arduous and extensive effort to characterize the spacecraft's magnetic field beforehand. This process involves either implementing a comprehensive magnetic controls plan to meticulously identify the field contribution from each individual subsystem, conducting elaborate swing testing of the entire spacecraft, or performing roll maneuvers in space, exploiting the fact that the total field remains constant along the spin plane. Only after this painstaking endeavor can accurate values for the coupling matrix, $\alpha$, be obtained, enabling the successful application of the algorithm.

#### 3.1.2. Frequency-Domain Gradiometry Filtering

Ream et al. (2021) introduced a new technique for removing stray magnetic fields generated by the spacecraft from the measurements of a magnetic gradiometer in the frequency domain. The technique applies a moving window to calculate the difference between the observed fields at two magnetometers on a boom, and uses two parameters, $n$ and $\delta b$, to detect the intervals where the spacecraft fields are active. An interval is classified as noisy when $\delta b/n$ meets a predefined threshold where $\delta b$ is the absolute change in magnetic field over a sliding window of length $n$. In those intervals, the technique analyzes the frequency spectra of the differenced field components and identifies the spectral peaks that correspond to the spacecraft fields. Those peaks are then automatically suppressed through reducing their amplitudes by a factor ranging from 20 to 100. The corrected frequency-domain signal is than inverted back into a time-series representing the ambient magnetic field signal.

The Ream method and the Ness method both use a magnetic gradiometer to eliminate spacecraft fields. However, the Ream technique works in the frequency domain while the Ness technique operates using spatial information. Additionally, the Ream method can handle multiple overlapping spacecraft fields, while the Ness method assumes a single effective dipole field.

#### 3.1.3. Principal-Component Gradiometry

The PiCoG algorithm is an advanced gradiometry technique used to remove stray magnetic field signals (Constantinescu et al., 2020). It works best with two or more magnetometers. Unlike the Ness et al. (1971) method, which assumes a specific magnetic field structure, PiCoG uses a different approach. PiCoG finds the direction of maximum variance, a process sometimes referred to as Maximum-Variance Analysis (MVA), in the

magnetometer data and applies a coordinate transform using Principal Component Analysis (PCA). The transformed magnetometer data are then used to estimate the coupling parameter, $\alpha$. This estimation is achieved through the following equation:

$$\alpha = \sqrt{\frac{\mathrm{Var}(B_x)}{\mathrm{Var}(\Delta B_x)}} \tag{2}$$

In this equation, $\mathrm{Var}(B_x)$, represents the variance of the magnetic field in the direction of maximum variance found through PCA, while $\mathrm{Var}(\Delta B_x)$ denotes the variance of the differenced magnetometer signals along that axis. In this method, $B_x$ represents the magnetic field component in the new coordinate system aligned with the direction of maximum variance, rather than the original x-direction of the spacecraft coordinate system. Because the rotation of the spacecraft affects the results of PCA, it must be performed on magnetometer signals transformed into a despun coordinate system.

Following the estimation of the coupling parameter from the magnetometer data in the transformed coordinate system, we can then proceed to recover the ambient magnetic field signal. This recovery is performed using the equation:

$$B'_k = B_k - \alpha\left(R^{-1}\right)_{kx}(R\Delta B)_x \tag{3}$$

In this equation, $k \in (1, 2, 3)$ and $R$ represents the transformation matrix.

The PiCoG algorithm can be applied iteratively to remove multiple disturbance sources using more than two sensors. This technique has been successfully implemented on board the Service Oriented Spacecraft Magnetometer instrument on the GEO-KOMPSAT-2A geostationary satellite, which delivers accurate magnetic field data in near-real time for space weather applications (Constantinescu et al., 2020).

### 3.1.4. Sheinker and Moldwin Gradiometry

Sheinker and Moldwin (2016) developed an adaptive gradiometry algorithm that does not make assumptions about the spacecraft magnetic field signal or the nature of the stray magnetic field interference itself. The algorithm assumes there is a single interference signal, $a(n)$, interfering with the ambient magnetic field signal, $x(n)$, where $n$ represents discrete time steps. The mixing system is defined as:

$$\begin{cases} b_1(n) = x(n) + a(n) + w_1(n) \\ b_2(n) = x(n) + ka(n) + w_2(n) \end{cases} \tag{4}$$

Where $b(n)$ are the magnetometer signals and $w(n)$ is the intrinsic noise of each magnetometer. The Sheinker and Moldwin (2016) method estimates the coupling coefficient $\hat{k}$ by correlating the differences between the two magnetometer signals. After $\hat{k}$ is estimated, the ambient magnetic field $x(n)$ can be restored as:

$$x(n) = \frac{\hat{k}b_1(n) - b_2(n)}{\hat{k} - 1} \tag{5}$$

This method does not assume anything about the stray field characteristics. However, it assumes there is only one interference source, which works well when the spacecraft field can be modeled as a single dipolar interference signal with one coupling coefficient. The method fails to remove multiple interference signals when that assumption is invalid.

### 3.1.5. Independent Component Analysis

Imajo et al. (2021) introduced an application of ICA to mitigate spacecraft interference in the magnetometer data collected from the Michibiki-1 satellite. ICA is an algorithm designed to separate signals based on their statistical independence. This algorithm operates under the assumption of a mixing system, where the magnetometer measurements, $b$, are considered a linear combination of source signals, $s$, as described by the following system:

$$b = Ks \tag{6}$$

In this equation, the matrix $K$ represents the mixing matrix, which specifies how each source signal contributes to each magnetometer's measurements. Through a series of iterative steps leveraging relationships between statistical independence, entropy, and Gaussian distributions, ICA seeks to find a set of vectors, $W$. These vectors are used to project $b$ into a space that maximizes the non-Gaussianity of $W^T b$. The matrix, $W$, can be inverted to find the original mixing matrix, $K$ (Hyvärinen & Oja, 2000).

It is important to note that the ICA algorithm has several limiting assumptions. It is a determined algorithm, meaning it cannot isolate more signals than there are measurement channels available. Additionally, the use of ICA necessitates that the source signals are independent and non-Gaussian.

### 3.1.6. Multichannel Singular Spectrum Analysis

Finley et al. (2023) applied M-SSA to distinguish stray magnetic field interference from geophysical magnetic field signals. Singular Spectrum Analysis (SSA) is a method designed to deconstruct time-series signals into their statistically meaningful components. M-SSA is an extension of SSA tailored to handle data from multiple measurement channels. This method involves a several-step algorithm that starts with the formulation of the trajectory matrix, denoted as $X$ from the noisy magnetometer data.

$$X = \begin{bmatrix} x_m(1) & x_m(2) & x_m(3) & \dots & x_m(K) \\ x_m(2) & x_m(3) & x_m(4) & \dots & x_m(K+1) \\ x_m(3) & x_m(4) & x_m(5) & \dots & x_m(K+2) \\ \vdots & \vdots & \vdots & \ddots & \vdots \\ x_m(L) & x_m(L+1) & x_m(L+2) & \dots & x_m(N) \end{bmatrix} \tag{7}$$

In this equation, the $L$ number of rows represent $K$-length lagged versions of the magnetometer signal, $x(n)$, that is of length $N$. The subscript, $m$, denotes the magnetometer. The trajectory matrix is used to define the Lag-Covariance matrix, $C$, such that.

$$C = \frac{1}{K} X^T X \tag{8}$$

The statistically significant signal components can be found from the lag-covariance matrix through taking an eigandecomposition of $C$. Finley et al. (2023) adds an additional step to identify interference signals through the correlation of the signals with the difference between the magnetometer measurements. M-SSA is a computationally expensive algorithm and relies on an approximation of the magnetometer interference to distinguish geophysical signals that may not always be valid. Additionally, the M-SSA algorithm's capability to separate overlapping signals is contingent upon asymptotic separability, a condition that necessitates both the input signal length and the analysis window length to approach infinity. This requirement is impractical for real-world computational systems and introduces a fundamental limitation (Golyandina et al., 2018).

### 3.1.7. Underdetermined Blind Source Separation

The UBSS algorithm is well-known in the fields of radar and acoustic signal processing. Hoffmann and Moldwin (2022) developed UBSS to separate stray magnetic field interference from natural magnetic field signals. The UBSS algorithm models the system of magnetometers and source signals with the following equation:

$$B = KS \tag{9}$$

Where $B$ is a vector of $m$ mixed magnetometer measurements, $S$ is a vector of $n$ source signals such that $m < n$, and $K$ is the underdetermined mixing matrix that defines the contribution of each source signal to each magnetometer.

The UBSS algorithm implemented by Hoffmann and Moldwin (2022) is a two-step process. First, it identifies the interference signals through cluster analysis. Second, it separates the interference signals through compressive sensing. The UBSS algorithm makes no assumptions about the magnitude, location, or characteristics of the interference signals, except that they are sparse in the time-frequency domain. The use of compressive sensing makes UBSS computationally expensive, although this algorithm can be parallelized.

#### 3.1.8. Wavelet-Adaptive Interference Cancellation for Underdetermined Platforms

The WAIC-UP algorithm is an extension of the algorithm by Sheinker and Moldwin (2016) to the wavelet domain. Hoffmann and Moldwin (2023) apply WAIC-UP by linearly transforming the mixed magnetometer measurements via a wavelet transform. The Sheinker and Moldwin (2016) algorithm is applied to each wavelet-scale to remove stray magnetic field interference. However, due to the shrinking cone of influence, the wavelet transform is not valid at lower frequencies, and WAIC-UP can not be applied. This makes the WAIC-UP algorithm a high-frequency interference removal algorithm. One positive aspect of WAIC-UP is that it is incredibly fast compared to UBSS and M-SSA, and has the potential for real time interference removal.

### 3.2. Benchmarks and Metrics

In this work, we evaluate the performance of algorithms in the MAGPRIME library using two benchmarks. The benchmarks are designed to facilitate the comparison of current and future interference removal algorithms. The benchmarks consist of Monte Carlo simulations of stray magnetic field interference in a 3U CubeSat (10 cm × 10 cm × 30 cm) volume. MAGPRIME is designed to work in tandem with the Magpylib library to simulate magnetic fields. Magpylib is used to create current loops that generate the stray magnetic fields. Previous work by Boschetti et al. (2012) used a similar approach to evaluate the worst case magnetic field of the Gravity Field and Steady-State Ocean Circulation Explorer (GOCE) satellite. Additionally, Park et al. (2022) used Magpylib to evaluate the magnetic cleanliness of the Korean Pathfinder Lunar Orbiter (KPLO) satellite. In this work we simulate both AC and DC interference, but do not take any conductive materials into account.

The first benchmark, denoted Benchmark A, simulates a gradiometry configuration commonly employed by modern spacecraft that depend on magnetometer measurements (Auster et al., 2008; Broadfoot et al., 2022; Kilcommons et al., 2017; Kivelson et al., 2023). Traditionally, this setup involves placing one sensor at the boom's end and another halfway down, with the presumption that both sensors reside within the far-field domain, thereby validating the single effective dipole assumption. In this benchmark, we adapt this traditional configuration to a more extreme scenario by placing one virtual magnetometer at the end of a 30 cm boom and another at the base of the boom in the near-field environment. A general guideline suggests employing a boom at least twice the length of the spacecraft's size when not utilizing interference removal algorithms. In our study, we deviate from this standard by using a 30 cm boom to assess the algorithms' effectiveness under these non-conforming conditions, which are more likely on a CubeSat. We sample each virtual magnetometers at 50 Hz for 100 s with 64-bit float precision and no additional intrinsic measurement noise.

In the second benchmark, denoted Benchmark B, we evaluate the performance of the magnetometers in a boomless configuration. The three virtual magnetometers are mounted on the bottom, top, and midsection of the bus of the CubeSat, sampled at 50 Hz for a 100-s window. While this boomless configuration has not been flown before, advancements in interference removal algorithms, as explored in works like Strabel et al. (2022) and Hoffmann et al. (2023), are expected to reduce the reliance on mechanical booms and lower the cost, risk, and complexity of magnetic field measurements in space. In each simulation, the interference source locations are randomized, maintaining a minimum distance of 1 cm from the bus-mounted magnetometers. An example configuration of the magnetometers, interference generators, and stray magnetic field structure for each benchmark is illustrated in Figure 2.

The stray magnetic field signals in our simulations are generated using four current loops with magnetic moments of $4.71 \times 10^{-2}\mathrm{Am}^2$ in Benchmark A and $3.14 \times 10^{-3}\mathrm{Am}^2$ in Benchmark B. These configurations can create field strengths of up to 18,570 nT and 1,238 nT, respectively, at a distance of 5 cm away from the current loop. The different magnetic moments were chosen to ensure sufficient interference levels at the end of the boom, and for the bus-mounted magnetometers to not exceed interference levels that typically cause saturation. For context, this level of magnetic field strength exceeds the 7,500 nT peak-to-peak stray magnetic field interference observed by

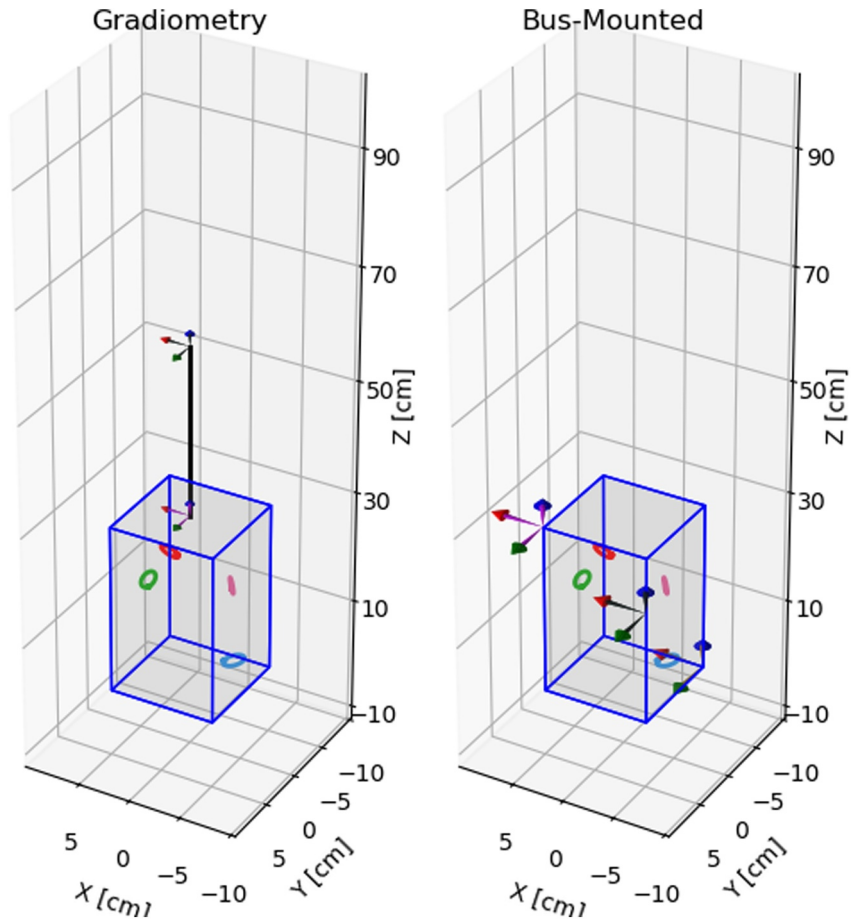


**Figure 2.** Visualization of CubeSat magnetometer configurations for magnetic field measurement benchmarks with magnetometers as tricolor vectors and dipole interference sources shown as current loops. Benchmark A, on the left, employs a traditional gradiometry setup with a 30 cm boom with virtual magnetometers sampled at 50 Hz over 100 s located at (0, 0, 30) cm and (0, 0, 60) cm from the CubeSat's origin at (0, 0, 0). Benchmark B, on the right, shows a boomless configuration with virtual magnetometers mounted directly on the CubeSat's bus at coordinates (5, 5, 30) cm, (−5, 5, 20) cm, and (−5, −5, 0) cm. All interference sources are placed at least 1 cm away from the nearest magnetometer.

the Ex Alta-1 CubeSat when its magnetometer was stowed, illustrating that our simulations operate within a realistic parameter space for bus-mounted magnetometers (Miles et al., 2016).

The four interference sources consist of real interference from the Michibiki-1 satellite, simulated reaction wheel interference with a shifting frequency, simulated arcjet interference, and a sawtooth signal with a frequency of 3 Hz that turns on and off randomly. The real stray magnetic field was a 24-hr sample of interference taken from the Michibiki-1 magnetometers on 23rd April 2012 (Imajo et al., 2021). The interference was calculated using difference between the inboard and outboard magnetometers to remove the ambient magnetic field signal. The Michibiki-1 interference is a 1 Hz signal that was randomized by selecting a random 5,000 data point slice. This method shifts the frequency of the Michibiki-1 interference, but preserves the spectral content of the original signal at a shifted frequency. The simulated arcjet interference is based of observations by Califf et al. (2020). The arcjet signal is created by randomly turning on and off a binary signal with constraints placed on the duration to make it resemble a true arcjet. The reaction wheel interference consists of a sine wave that shifts down to a random frequency using a chirp signal, and returns to the same fundamental frequency (Loto'aniu et al., 2019). This resembles an attitude determination maneuver of a spacecraft where the angular momentum of the reaction wheels is used to modulate the spacecrafts orientation. These four signals represent a variety of interference sources that a spacecraft might produce. Additionally, their spectral content is incredibly broadband, so that their combination creates a very pathological case for the application of interference removal algorithms.

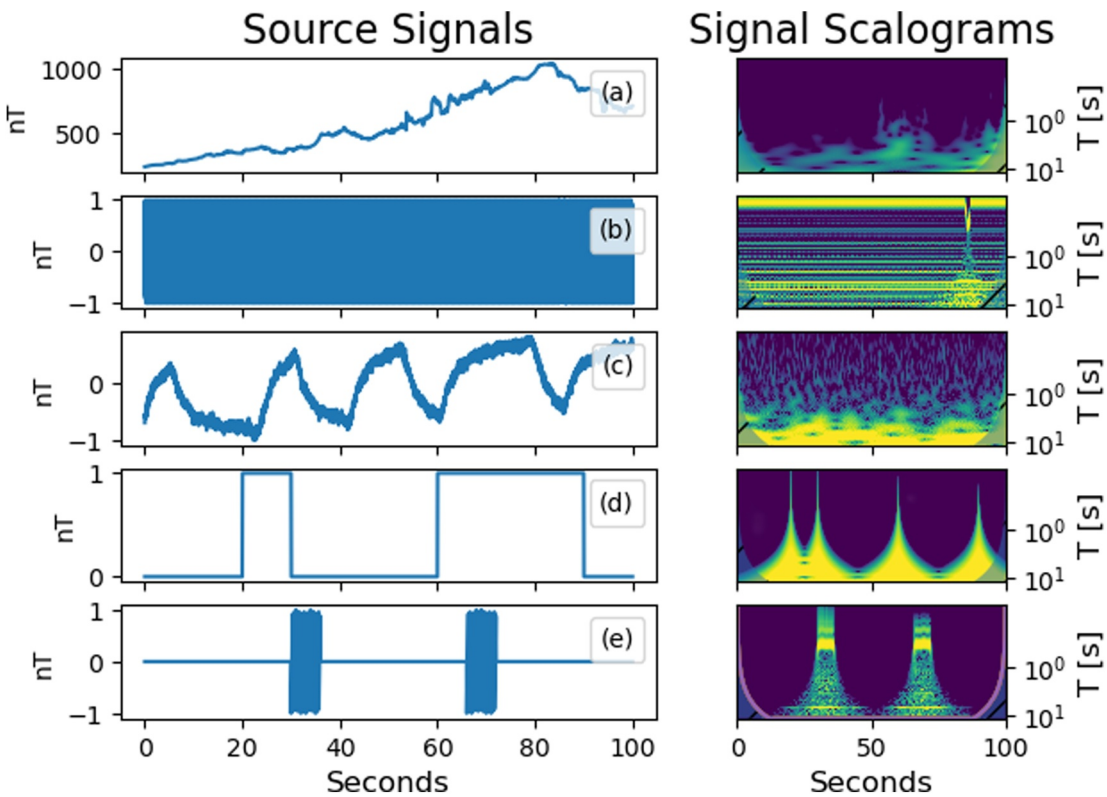


**Figure 3.** Five source signals sampled at 50 Hz. Panel (a) shows the natural magnetic field signal taken from the Swarm A Spacecraft on 17th March 2015. Panel (b) shows the simulated reaction wheel interference with a shifting frequency. Panel (c) shows the real interference from the Michibiki-1 satellite. Panel (d) shows the simulated arcjet interference. Panel (e) shows the sawtooth signal with a frequency of 3 Hz that turns on and off randomly. Each time series signal except for the ambient magnetic field signal is normalized. The second column shows the wavelet scalogram of each source signal. The y-axis is the period of the signal in seconds. The coloring shows the normalized amplitude of the detrended signals.

Finally, the overarching goal of these benchmarks is to evaluate the ability of algorithms to separate ambient magnetic field signals from stray magnetic field interference. To simulate a realistic ambient magnetic field signal that a CubeSat would measure in low Earth orbit, we use real magnetometer data from the Swarm A spacecraft (Friis-Christensen et al., 2008). Specifically, we selected a geomagnetic perturbation signal recorded on 17 March 2015 between 8:53 and 8:55 UTC. During this window, Swarm A was flying above Earth's southern auroral zone between the 69th and 76th southern latitude parallel. This auroral magnetometer data provides a complex natural ambient signal on top of which we can overlay the simulated spacecraft interference sources.

By benchmarking algorithms on this combined ambient and stray field data, we can quantify the ability to recover the underlying ambient signal in a realistic interference environment. Example spectra for the four randomized source signals used in this experiment and the ambient magnetic field signal from Swarm A are shown in Figure 3.

To quantify the performance of algorithms for separating ambient and stray magnetic field signals, we employ three distinct metrics: Pearson correlation coefficient, root mean square error (RMSE), and signal-to-noise ratio (SNR).

The Pearson correlation coefficient, calculated as per Equation 10, measures the similarity between the cleaned signal ($y_i$) and the true ambient magnetic field ($x_i$). Correlation excels at measuring the removal of variable stray magnetic field signals because it is detrended in its calculation, where $\bar{x}$ and $\bar{y}$ are the means of true and estimated signals, and $n$ is the number of data points.

$$\rho = \frac{\sum_{i=1}^{n}(x_i - \bar{x})(y_i - \bar{y})}{\sqrt{\sum_{i=1}^{n}(x_i - \bar{x})^2}\sqrt{\sum_{i=1}^{n}(y_i - \bar{y})^2}} \tag{10}$$

RMSE, defined in Equation 11, quantifies the absolute error between the processed signal ($y_i$) and the true ambient field ($x_i$), offering a direct measure of the algorithm's accuracy.

$$\text{RMSE (nT)} = \sqrt{\frac{\sum_{i=1}^{n}(x_i - y_i)^2}{n}} \tag{11}$$

Lastly, SNR, as described in Equation 12, compares the power of the remaining ambient signal ($x_i$) to the noise level in the cleaned signal, providing insight into the relative error and the efficacy of the algorithm in preserving the true signal. Here, $\bar{x}$ is the mean of the true ambient signal values, and $n$ is the number of data points.

$$\text{SNR (dB)} = 10\log_{10}\frac{\sum_{i=1}^{n}(x_i - \bar{x})^2}{\sum_{i=1}^{n}(x_i - y_i)^2} \tag{12}$$

## 4. Results

In this study, we rigorously assess the capabilities of eight unique algorithms from the MAGPRIME library, targeting their performance in filtering interference from triaxial magnetometer data. Utilizing Monte Carlo simulations, we simulate two distinct magnetometer configurations, dual magnetometer gradiometry and a novel three magnetometer boomless setup, as outlined in Section 3.2. Each configuration was subjected to 100 simulations, yielding a data set that enabled us to conduct an extensive and detailed statistical analysis of the algorithms' efficacy under diverse and challenging conditions. The simulations were randomized through randomly placing and orienting the interference soures, as well as randomizing the content of the interference signals. Several algorithms are computationally expensive, so these simulations were run on the University of Michigan's Great Lakes high performance computing cluster.

The results are structured to first present a detailed analysis of each algorithm's performance under the gradiometry setup (Benchmark A), followed by their performance in the boomless configuration (Benchmark B). Within each section, we explore the algorithms' effectiveness using metrics described in Section 3.2. This structured presentation allows for a clear and comparative understanding of each algorithm's strengths and limitations in different scenarios. This section will delve into the specifics of these results, offering insights into the performance of each algorithm under varying conditions and their potential applicability in real-world space physics scenarios.

In the simulations, the ICA, WAIC-UP, and M-SSA algorithms were detrended with a uniform filter of N = 500 data points before being applied to remove stray magnetic field signals as outlined in their respective literature (Finley et al., 2023; Hoffmann & Moldwin, 2023; Imajo et al., 2021). The total signal length for this experiment spans 100 s, equivalent to 5,000 data points, making the filter window one-tenth of the overall signal. It is important to note that the parameters of these algorithms were not individually optimized for each simulation, so randomized testing may not provide a clear understanding of their performance when manually tuned to a spacecraft. However, the coupling coefficients for the Ness et al. (1971) algorithm were precisely calculated from the simulated magnetic field, offering a potentially more accurate estimation than typical laboratory characterizations.

### 4.1. Benchmark A: Gradiometry Configuration

Benchmark A evaluates the interference removal algorithms in a 3U CubeSat context, featuring a dual-magnetometer setup with one sensor on the end of a 30 cm boom and another at the boom's base. Within the CubeSat's confines, four dipole interference sources are randomly placed, requiring a minimum distance of 1 cm from the base-mounted magnetometer. The plot in Figure 4 depicts the composite ambient and stray magnetic field signals recorded at the boom's base for one of the simulation runs. Each panel illustrates the respective x-axis, y-axis, and z-axis mixed signals in blue, overlayed with the true magnetic field signal in orange. The data prominently features high-frequency oscillations from reaction-wheel interference from 10 to 20 s, alongside a strong square wave pattern from 20 to 30 s and 60–90 s, which mimics the interference signature of GOES-16 arcjet firing (Califf et al., 2020; Carter et al., 2016).

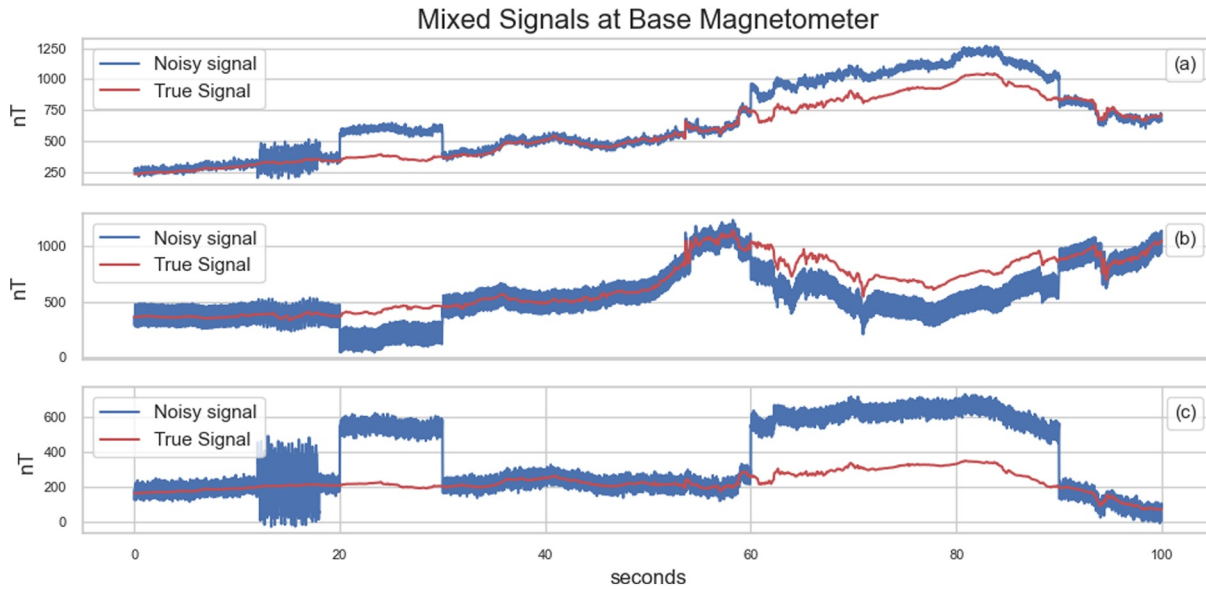


**Figure 4.** Mixed ambient and stray magnetic field signals over a 100-s interval from the magnetometer at the base of the boom in the 3U CubeSat gradiometry configuration. Panels (a–c) represent the mixed signals for the x-axis, y-axis, and z-axis, respectively, with the noisy signals displayed in blue and the true ambient magnetic fields overlaid in orange. The limits of the y-scale in each panel is adjusted to the size of the signal.

Figure 5 shows the noisy magnetometer measurements from the same simulation as in Figure 4 as seen at the end of the boom. The magnitude of the interference sources at the end of the boom are reduced to about 20 nT peak to peak from hundreds of nanoTeslas observed at the base. This notable attenuation of interference highlights the efficacy of the boom placement in mitigating electromagnetic interference without the use of any interference removal.

Figure 6 presents the RMSE distributions from the z-axis signals processed by each MAGPRIME algorithm, alongside the base and boom magnetometers' RMSE for a comparative baseline without any cleaning applied. Notably, the boom-mounted magnetometer exhibited exceptionally low RMSE values even in the absence of a cleaning algorithm, underscoring its inherent interference reduction capability due to its positioning. The base

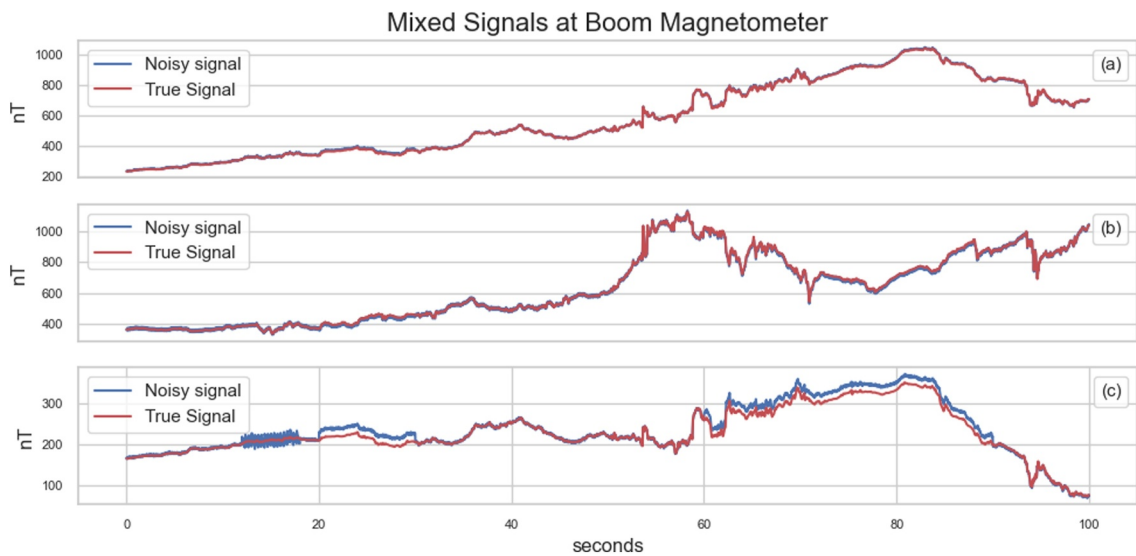


**Figure 5.** Mixed ambient and stray magnetic field signals over a 100-s interval from the magnetometer at the end of the boom in the 3U CubeSat gradiometry configuration. Panels (a–c) represent the mixed signals for the x-axis, y-axis, and z-axis, respectively, with the noisy signals displayed in blue and the true ambient magnetic fields overlaid in orange. The limits of the y-scale in each panel is adjusted to the size of the signal.

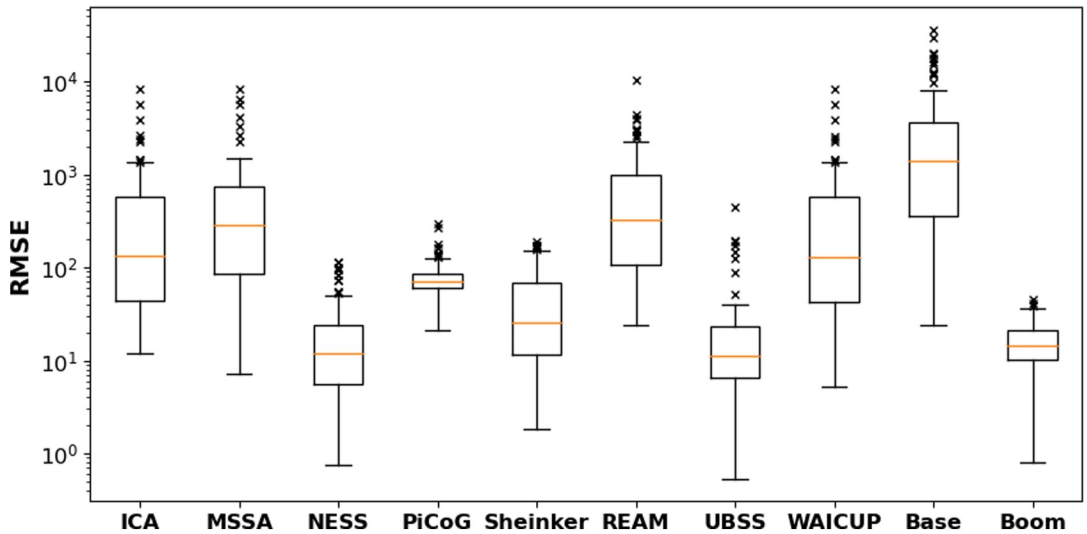


**Figure 6.** A box and whisker plot illustrating the RMSE for each MAGPRIME algorithm evaluated on the z-axis signals. The plot also includes the RMSE for the boom and base magnetometers to serve as benchmarks. The results highlight the superior interference reduction performance of the UBSS and Ness algorithms, which outperformed the naturally lower error levels of the boom-mounted magnetometer.

magnetometer's median RMSE was approximately 1,400 nT while the boom's median RMSE was close to 14 nT. The UBSS and Ness algorithms surpassed the boom magnetometer's performance, each achieving a median RMSE that was nearly 11 nT.

However, since the M-SSA, ICA, and WAIC-UP detrend the signals before interference removal, metrics such as RMSE and SNR might not fully capture their capability. These algorithms excel at mitigating higher frequency interference, however, lower frequency interference can be reintroduced after retrending the data. In this case, the correlation coefficient becomes a more accurate indicator of their performance because it removes the mean of each signal in its calculation.

The processed x-axis and y-axis signals from ICA, M-SSA, Ness, Sheinker, UBSS, and WAIC-UP exhibit median correlations exceeding 0.8, as fully detailed in Table 1. However, as shown in Figure 7, only the Sheinker, UBSS, and Ness algorithms achieve a median correlation above 0.9 in the z-axis. This discrepancy in correlations for the z-axis compared to the x and y axes can be attributed to the characteristics of the test data set. In Benchmark A, the base magnetometer with no interference removal has a much worse correlation in the z-axis than in the x and y axes. Consequently, the poorer correlation results of ICA, MSSA, and WAIC-UP in the z-axis reflect their sensitivity to the interference levels at the base magnetometer, whereas Ness and UBSS demonstrate robustness against this interference. Notably, the unprocessed boom magnetometer data achieved an almost perfect

**Table 1**
*Median Results for Gradiometry Configuration*

| Metric | | ICA | MSSA | Ness | PiCoG | Sheinker | Ream | UBSS | WAIC-UP | Base | Boom |
|---|---|---|---|---|---|---|---|---|---|---|---|
| RMSE | X | 81.53 | 136.37 | 5.45 | 52.79 | 66.41 | 259.69 | 7.25 | 77.38 | 773.30 | 7.47 |
| | Y | 94.20 | 133.80 | 5.49 | 128.85 | 94.80 | 247.05 | 8.41 | 72.38 | 720.81 | 6.74 |
| | Z | 131.91 | 288.11 | 11.97 | 69.97 | 25.85 | 322.21 | 11.29 | 130.64 | 1,389.38 | 14.42 |
| Corr | X | 0.9662 | 0.8909 | 0.9998 | 0.9823 | 0.9617 | 0.0988 | 0.9997 | 0.9753 | 0.4077 | 0.9996 |
| | Y | 0.9302 | 0.8878 | 0.9997 | 0.9048 | 0.9235 | 0.1419 | 0.9995 | 0.9664 | 0.4597 | 0.9996 |
| | Z | 0.4450 | 0.3769 | 0.9827 | 0.6533 | 0.9176 | 0.0416 | 0.9854 | 0.4859 | 0.0833 | 0.9738 |
| SNR | X | 9.41 | 4.95 | 32.92 | 13.19 | 11.20 | −0.65 | 30.43 | 9.87 | −10.13 | 30.18 |
| | Y | 7.57 | 4.52 | 32.25 | 4.85 | 7.51 | −0.81 | 28.55 | 9.86 | −10.11 | 30.48 |
| | Z | −7.11 | −13.89 | 13.74 | −1.61 | 7.05 | −14.87 | 14.24 | −7.02 | −27.56 | 12.12 |

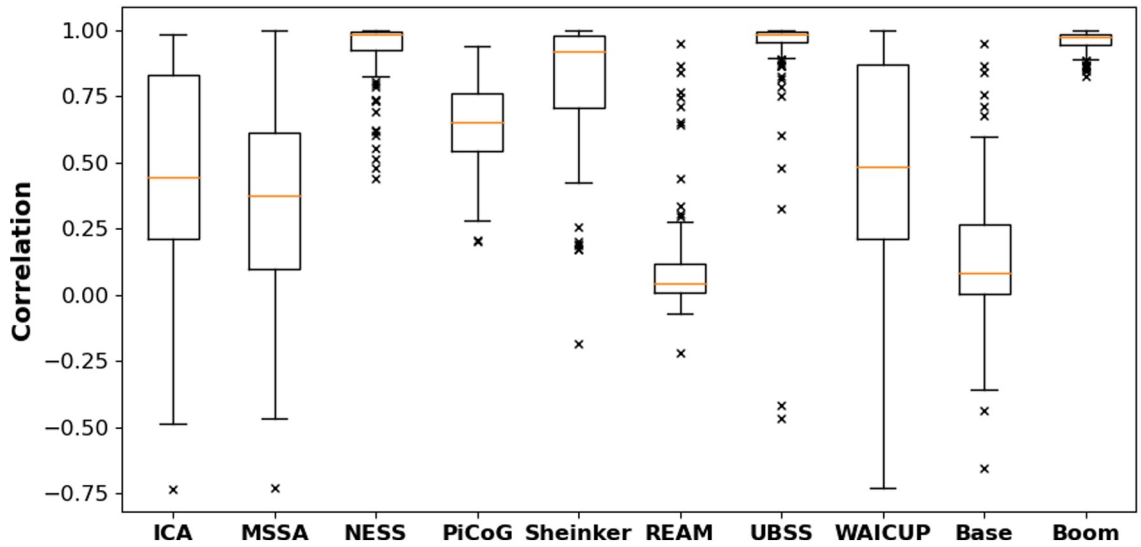


**Figure 7.** Distribution of correlation coefficients for the z-axis signals processed by MAGPRIME algorithms, compared with unprocessed signals from the boom and base magnetometers. High correlation values indicate effective interference removal, with ICA, M-SSA, Sheinker, and WAIC-UP showing strong performance. The boom magnetometer's baseline correlation is nearly perfect, with only UBSS and Ness achieving comparable results.

correlation of 0.97, a level only matched by UBSS and Ness, underscoring their superior ability to filter both DC and AC interference in gradiometry setups with broadband interference.

Next, we evaluated the full vector SNR for each algorithm's processed signal. The SNR, a critical metric that quantifies the power ratio of the ambient magnetic field signal to the stray magnetic field signal, indicates the algorithm's effectiveness in enhancing the true signal while suppressing interference. Figure 8 displays the SNR values' probability density functions for the x, y, and z-axis signals processed by each algorithm. This visualization allows for a comparison of each algorithm's interference reduction capabilities and their performance consistency across different axes in a gradiometry configuration.

The data illustrated in Figure 8 showcases the impressive performance of the boom magnetometer, which achieves median SNRs of 30.18, 30.48, and 12.12 dB for the x, y, and z-axes, respectively. The standard deviation for each axis is about 5 dB. While UBSS excels over the boom in median SNR on the x and z axes, it exhibits a wider standard deviation, close to 10 dB. Ness, on the other hand, slightly surpasses the boom magnetometer in terms of SNR across all axes but has marginally larger standard deviations compared to UBSS. The other algorithms assessed fall short of the boom magnetometer's SNRs. These outcomes indicate that the use of a short boom on a 3U CubeSat can provide remarkably clean magnetometer data, assuming the CubeSat has a sufficiently minimized magnetic moment. UBSS and Ness generally outperform or match the boom magnetometer's cleaning efficacy, with the exception of the UBSS's x-axis signal, which has a slightly elevated RMSE and a lower SNR compared to the boom magnetometer. Table 1 presents the median tri-axial results of each metric for each algorithm, providing a comprehensive view of their performance.

### 4.2. Benchmark B: Boomless Configuration

In Benchmark B, we focus on evaluating interference removal algorithms in a boomless magnetometer setup for CubeSats, a potential cost-effective alternative to traditional designs (Strabel et al., 2022). This setup comprises three virtual magnetometers, M1, M2, and M3, located at the top, middle, and bottom of the CubeSat's bus. The boomless approach simplifies the CubeSat's structure and aims to reduce costs in space-based magnetic field measurements.

Figure 9 presents the time series signals from the M1 magnetometer at the CubeSat's top. These signals combine ambient and stray magnetic fields, providing raw data for algorithmic processing to discern the true magnetic field. The algorithms' effectiveness in this boomless context will inform the feasibility of such designs in future CubeSat missions. However, the presence of broadband and random normal interference in these signals presents a potentially more challenging environment than typical operational scenarios.

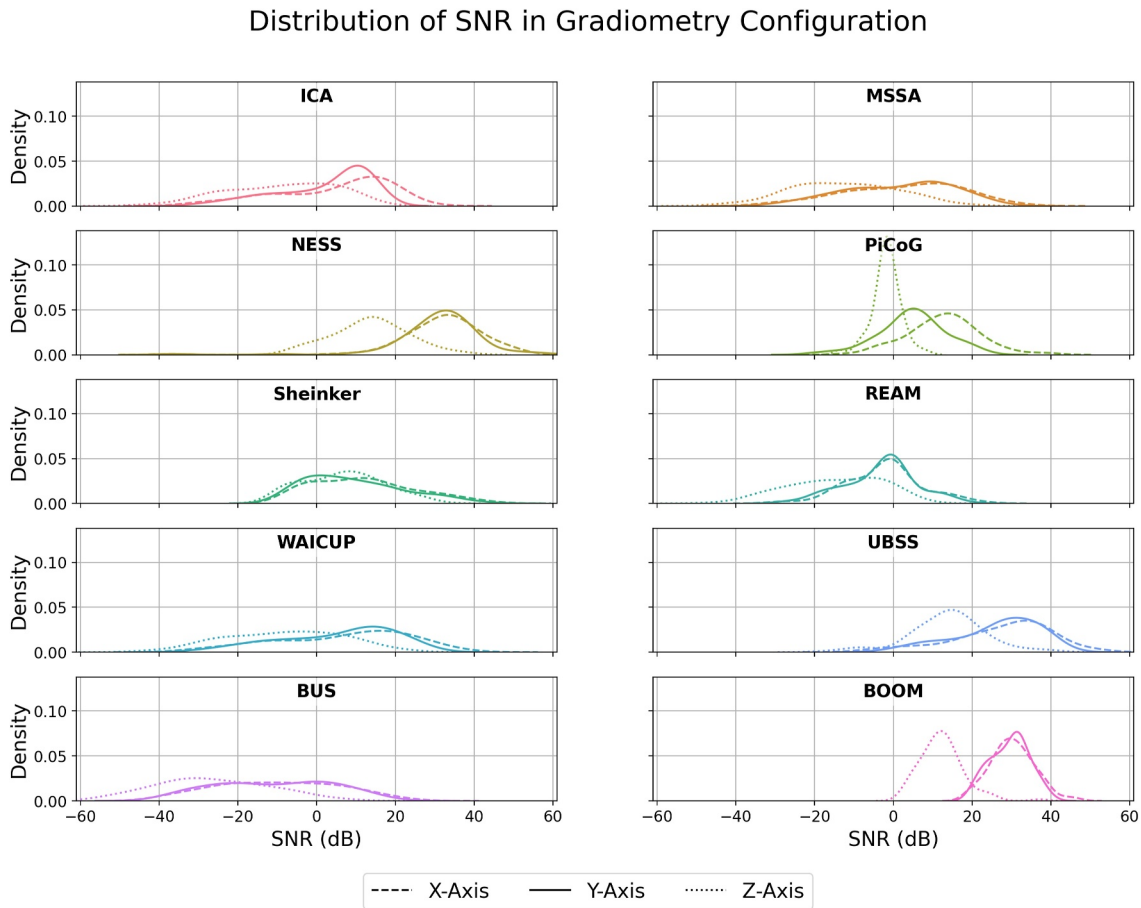


**Figure 8.** Probability density functions of the SNR values for each axis of each algorithm in the gradiometry configuration. Each subplot corresponds to a different algorithm, with the SNR distribution for the x, y, and z axes displayed in dashed, solid and dotted lines respectively.

We applied each interference removal algorithm to the noisy magnetometer data shown in Figure 9, along with data from 99 additional randomized simulations. The resulting RMSEs for the z-axis signals in the boomless configuration are depicted in Figure 10 through a box and whisker plot. Algorithms such as Ness, Sheinker, Ream, and PiCoG, which are specifically designed for dual-magnetometer setups, were implemented using data from only the top (M1) and middle (M2) magnetometers.

The results in Figure 10 show that UBSS had the greatest reduction in median RMSE down to 12 nT. UBSS leads every other algorithm with the lowest median RMSE and 25th percentile RMSE below 10 nT. WAIC-UP had the next lowest median RMSE of 17 nT followed by M-SSA. Other algorithms display higher RMSE values compared to the least noisy magnetometer (M1).

Figure 11 shows the correlation of each of the algorithms cleaned z-axis signal with the ambient magnetic field signal. ICA, M-SSA, and WAIC-UP each show correlation above 0.9 with a very small interquartile range. This indicates that they are very consistent at recovering the variable magnetic field signal. However, similar to Benchmark A, each of these algorithms had a high RMSE which suggests that the retrending process adds a DC offset to the cleaned signals. UBSS stands out with the highest median correlation of 0.98, and the smallest interquartile range.

Figure 12 presents the distribution of SNR values for each axis, measured by the algorithms in the boomless setup. ICA and WAIC-UP show particularly narrow distributions, signaling their ability to consistently achieve similar SNRs across multiple simulations. In the z-axis, UBSS and WAIC-UP stand out and achieved the highest SNRs of 13.76 and 10.67 dB, respectively, which markedly exceeds the SNR of uncleaned signals that range from 0 to 7 dB. This superior performance of UBSS and WAIC-UP demonstrates their effectiveness in enhancing signal

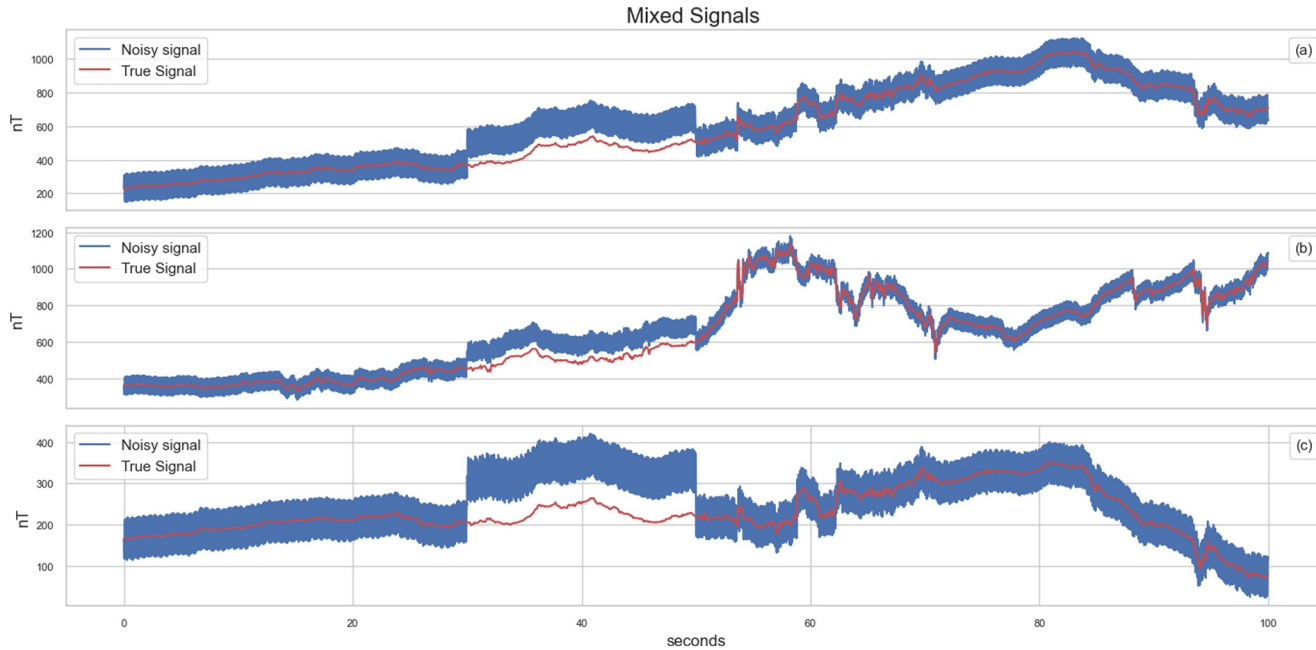


**Figure 9.** Time series representation of noisy signals captured by the virtual magnetometers in the boomless CubeSat configuration. This figure illustrates the complexity of the ambient and stray magnetic fields the algorithms are tasked to decipher. This benchmark serves as a basis for evaluating the algorithms' proficiency in a simulated worst-case interference scenario. The limits of the y-scale in each panel is adjusted to the size of the signal.

clarity in the boomless configuration. M-SSA also performed commendably, registering marginally higher SNRs than the least noisy magnetometer in two axes, while ICA did so in one axis. Conversely, Ness, Sheinker, and Ream algorithms exhibit distributions that align closely or fall short of the SNR levels of the least noisy magnetometer. Given that these algorithms are tailored for use with magnetometers configured in a gradiometry setup, their performance within this boomless context aligns with expectations.

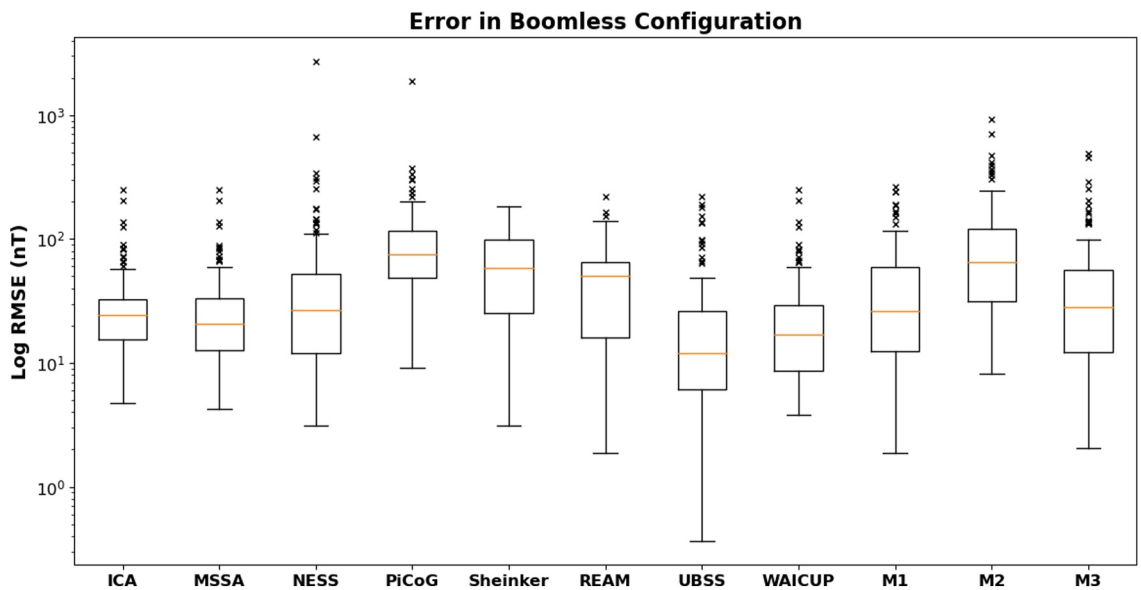


**Figure 10.** Distribution of the z-axis RMSE values for the cleaned signals from each interference removal algorithm tested in the boomless CubeSat configuration. The M1, M2, and M3 magnetometers show the raw RMSE of the top, middle, and bottom magnetometers respectively. The RMSE is shown in log scale to accentuate the difference between results.

10.1029/2024EA003675

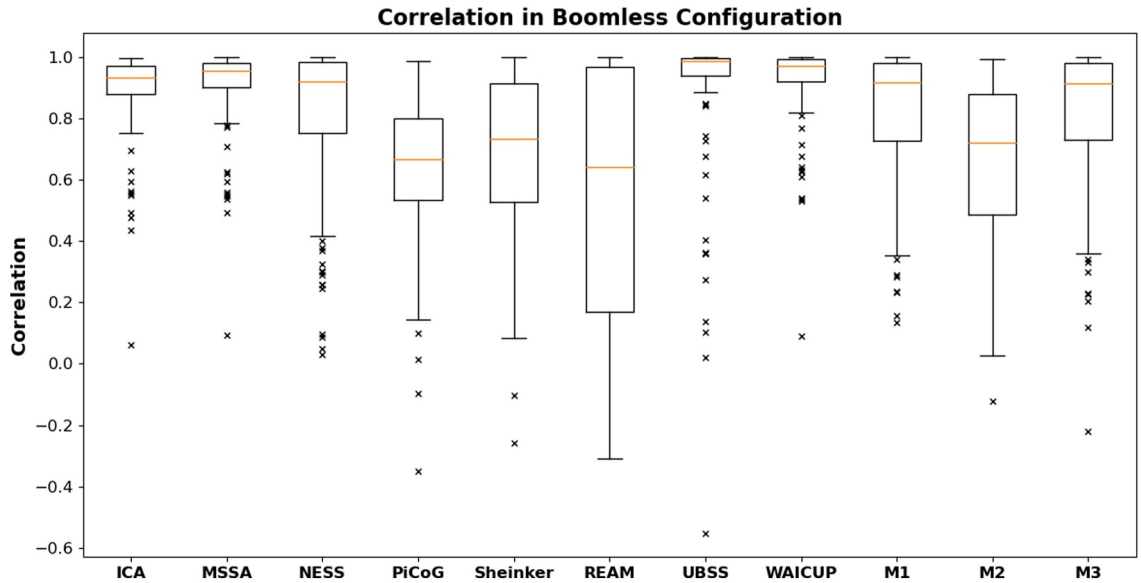


**Figure 11.** Distribution of correlation coefficients for the z-axis signals processed by MAGPRIME algorithms, compared with unprocessed signals from bus-mounted magnetometers. ICA, M-SSA, UBSS, and WAIC-UP each show high correlations and a small interquartile range.

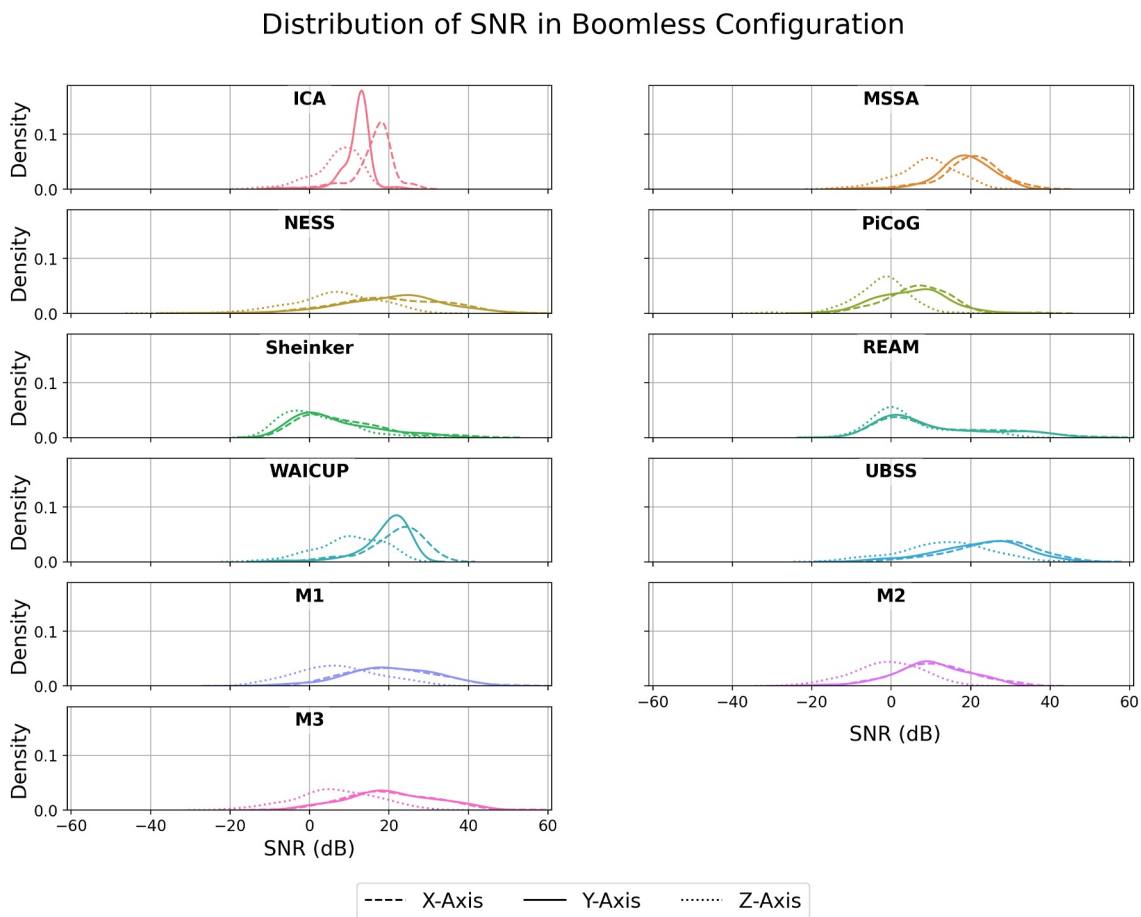


**Figure 12.** Probability density functions for SNR values of each interference removal algorithm across the x, y, and z axes in the boomless configuration. The distributions highlight the variability in performance, with some algorithms consistently achieving higher SNRs indicative of more effective interference reduction capabilities.

**Table 2**
*Median Results for Boomless Configuration*

| Metric | | ICA | MSSA | Ness | PiCoG | Sheinker | Ream | UBSS | Waicup | M1 | M2 | M3 |
|---|---|---|---|---|---|---|---|---|---|---|---|---|
| RMSE | X | 31.49 | 21.34 | 24.69 | 108.14 | 135.05 | 119.51 | 10.82 | 16.88 | 23.93 | 72.48 | 25.42 |
| | Y | 51.47 | 25.70 | 16.47 | 121.25 | 155.11 | 145.69 | 14.40 | 20.50 | 22.91 | 72.55 | 24.60 |
| | Z | 24.21 | 20.71 | 26.83 | 74.68 | 58.39 | 50.00 | 11.93 | 17.02 | 26.23 | 65.18 | 28.38 |
| Corr | X | 0.9931 | 0.9966 | 0.9959 | 0.9321 | 0.9089 | 0.8850 | 0.9992 | 0.9984 | 0.9955 | 0.9708 | 0.9954 |
| | Y | 0.9751 | 0.9956 | 0.9975 | 0.9124 | 0.8357 | 0.7863 | 0.9987 | 0.9973 | 0.9961 | 0.9605 | 0.9958 |
| | Z | 0.9327 | 0.9542 | 0.9216 | 0.6659 | 0.7318 | 0.6412 | 0.9866 | 0.9700 | 0.9182 | 0.7192 | 0.9124 |
| SNR | X | 17.68 | 21.05 | 19.79 | 6.96 | 5.03 | 6.10 | 26.95 | 23.09 | 20.06 | 10.44 | 19.54 |
| | Y | 12.82 | 18.85 | 22.72 | 5.40 | 3.24 | 3.78 | 23.89 | 20.81 | 19.85 | 9.84 | 19.23 |
| | Z | 7.61 | 8.97 | 6.72 | −2.17 | −0.03 | 1.31 | 13.76 | 10.67 | 6.92 | −0.99 | 6.23 |

Table 2 provides a summary of the median results of each metric for each algorithm across all three axes in the boomless configuration. The RMSE values confirm the superior performance of the UBSS algorithm, which consistently achieved the lowest median RMSE across all axes, followed closely by WAIC-UP and M-SSA. Correlation coefficients remain high for UBSS and WAIC-UP, reaffirming their effective alignment with the variable ambient field signal. SNR values further delineate the hierarchy of algorithm performance, with UBSS achieving the highest median SNR, especially on the x-axis. The consistency of UBSS across these metrics, coupled with the high correlation and SNR values, underscores its potential for practical application in space missions utilizing a boomless CubeSat design. WAIC-UP and MSSA also emerge as reliable alternatives, with their performance being significantly better than the least noisy magnetometer (M1) in multiple aspects.

## 5. Discussion and Future Work

In this study, we introduce the MAGPRIME Python library, which consolidates various magnetic interference removal algorithms into a user-friendly platform for scientists and engineers. We have developed two benchmarks to assess the effectiveness of the algorithms within the MAGPRIME library. Benchmark A involves positioning two magnetometers collinearly at the base and tip of a 30 cm mechanical boom attached to a 3U spacecraft, as depicted in Figure 2. We conducted 100 simulations with four dipolar interference sources randomly distributed within the CubeSat's volume. Each interference source simulates stray magnetic field interference from various sources, including the GOES-16 satellite and the Michibiki-1 satellite, as illustrated in Figure 3.

We tested the eight algorithms in the MAGPRIME library against these interference scenarios, evaluating them using metrics such as RMSE, SNR, and correlation, and compared them to the raw triaxial magnetometer signals. Our analysis showed that the unprocessed magnetometer on the boom performed remarkably well, with a median RMSE of nearly 7.47 nT for the x-axis, 6.74 nT for the y-axis, and 14.42 nT for the z-axis, significantly better than the base magnetometer's 773.30 nT for X, 720.81 nT for Y, and 1,389.38 nT for Z. This finding reinforces the established understanding that using a boom is the gold standard in spacecraft magnetometry; however, the quality of the data depends on the amplitude and characteristics of the effective spacecraft dipole and the actual boom length. Interestingly, both the modern UBSS algorithm and the traditional gradiometry algorithm, as described by Ness et al. (1971), either matched or surpassed the boom's performance in terms of SNR, correlation, or RMSE. This suggests that the Ness et al. (1971) algorithm is highly effective when used with a sufficiently long boom and an accurately characterized coupling matrix. In contrast, the UBSS algorithm does not require prior knowledge of the spacecraft's magnetic environment and matched the performance of the Ness et al. (1971) algorithm. This makes it a viable option when coupling coefficients are challenging to determine or subject to change, and it has significant implications for reducing the requirements for magnetic cleanliness and characterization in spacecraft design.

Some of the algorithms we tested require preprocessing to remove low-frequency trends, which could potentially skew the SNR and RMSE metrics. During our correlation analysis, which used a detrended approach, we found that the WAIC-UP, M-SSA, and ICA algorithms all achieved high correlations exceeding 0.9. Specifically, the WAIC-UP algorithm exhibited outstanding correlation scores, registering above 0.9753 for the x-axis, 0.9664 for

the y-axis, and a lower 0.4859 for the z-axis. Transitioning to the UBSS and Ness algorithms revealed an even higher level of performance. Ness, in particular, showed an exceptional alignment with the true signal, achieving correlations of 0.9998 for the x-axis, 0.9997 for the y-axis, and 0.9827 for the z-axis, nearly matching the scores of UBSS, which achieved 0.9997 for X, 0.9995 for Y, and 0.9854 for Z. The boom's correlations were similarly impressive, scoring 0.9996 on both the X and Y axes, and 0.9738 on the Z axis. These results clearly highlighted both UBSS and Ness, alongside the use of a boom, as the top-performing solutions in our Benchmark A analysis.

In Benchmark B, we evaluated the same interference signals used in Benchmark A but within a boomless setup. This setup involved mounting magnetometers at the top, middle, and bottom of a 3U CubeSat, as depicted in Figure 2. While bus-mounted magnetometers offer a cost-effective alternative to boom-mounted ones, they are more susceptible to stray magnetic field interference. In our 100 randomized simulations, the unprocessed magnetometer readings showed median RMSEs between 22 and 76 nT. We ensured that no interference source was positioned close enough to a magnetometer to generate excessively high magnetic field magnitudes.

We applied algorithms designed for dual magnetometers, such as Ness, PiCoG, Sheinker, and Ream, to the top (M1) and middle (M2) magnetometers. The analysis revealed that on one axis each, Ness and ICA outperformed the least noisy magnetometer. M-SSA excelled on two axes, whereas WAIC-UP and UBSS surpassed the performance on all three axes. Notably, UBSS achieved the most substantial reduction in RMSE, bringing it down to 10–15 nT for each axis, while WAIC-UP's improvement was more modest, with RMSEs ranging from 17 to 21 nT per axis. The median correlation and SNR results mirrored these RMSE findings. An in-depth analysis of the SNR distribution highlighted ICA's consistency, closely followed by WAIC-UP. While neither ICA nor WAIC-UP could best UBSS in median RMSE, they consistently achieved comparable SNRs across varied experiments.

The outcomes from Benchmark B indicate that UBSS is not only the most effective interference removal algorithm in this scenario but also a strong competitor to Ness from Benchmark A. This benchmark demonstrates the viability of boomless magnetometry. Even without optimal magnetometer placement or magnetic cleanliness, using a boomless setup with UBSS can reduce stray magnetic field interference to a significantly lower level. While this level may not be adequate for certain heliophysical studies, such as analyzing small amplitude MHD waves or planetary induction, it is acceptable for many other types of investigations of large amplitude phenomena such as field-aligned currents at low altitudes, dipolarization, and magnetopause crossings in geostationary and higher apogee orbits. The emergence of boomless magnetometry has the potential to significantly influence space science by enabling the mass production of low-cost space science satellites. A summary of each algorithm's requirements and the ranked RMSE results for each benchmark is shown in Table 3.

The two benchmarks demonstrate MAGPRIME's potential for integration into the design process of space exploration missions. When used alongside magnetic field simulation software like Magpylib, MAGPRIME enables the exploration of design trade-offs. During a spacecraft's design phase, it can determine the optimal minimum boom length and the most effective magnetometer placement. This is shown in the best case of Benchmark B where UBSS achieved sub-nanotesla accuracy. These results indicate that boomless high-fidelity magnetic field measurements can be achieved with strategic knowledge of interference source locations and optimized magnetometer placement. If specific design constraints, such as boom length, cannot be met, MAGPRIME can identify the algorithm best suited to the spacecraft's unique design. Furthermore, the MAGPRIME library can be adapted for use in a mission's data processing pipeline to analyze magnetometer data. Overall, MAGPRIME is a valuable tool that supports spacecraft missions from the research and design stages through to operational phases.

The outcomes of these experiments come with several notable limitations due to their randomized nature. First, some algorithms require detrending of magnetometer signals to effectively clean high-frequency stray magnetic interference. The signals in our study were retrended using a basic mean trend method, which likely reintroduced low-frequency interference from sources like arcjet and Michibiki interference signals into the cleaned signal. Therefore, correlation, which detrends both the estimated and true magnetic field signals in its calculation, emerges as a more accurate measure of these algorithms' efficacy. Another limitation is the tunability of algorithm-specific parameters to match the unique magnetic field signature of a spacecraft. In our benchmarks, we did not adjust these parameters for each randomized simulation, possibly underrepresenting the algorithms' true potential in real-world scenarios. Future work could involve taking the worst-case and median-case interference scenarios and running the algorithms with tuned parameters. This approach would provide a clearer understanding of how different algorithms might perform in practical applications. Additionally, the test signals

**Table 3**
*Comparison of Magnetometer Interference Removal Algorithms*

| Algorithm | Boom | Spectrum suitability | Domain | Streamable | Axis | Benchmark A Rank | Benchmark B Rank | Assumptions |
|---|---|---|---|---|---|---|---|---|
| Gradiometry | Long | Broad | Time | Yes | Monoaxial | 1 | 4 | Single effective dipole interference signal |
| Frequency-domain Gradiometry | Long | High | Frequency | No | Monoaxial | 8 | 7 | Interference has no spectral overlap with the ambient magnetic field signal. Interference is intermittent in the time-domain |
| PiCoG | Long/Short | Broad | Time | No | Triaxial | 4 | 6 | Interference sources appear orthogonal at magnetometers. Magnetometer data is despun |
| Sheinker and Moldwin | Long/Short | Broad | Time | Yes | Monoaxial | 3 | 8 | Single interference source |
| ICA | Boomless | Broad | Time | No | Triaxial | 6 | 5 | Non-Gaussian Interference, Statistical Independence, and Determined System. Magnetometer data is despun |
| M-SSA | Boomless | Broad | Time | No | Monoaxial | 7 | 3 | Statistical significance and sufficient window length |
| UBSS | Boomless | Broad | Time-Frequency | No | Monoaxial | 2 | 1 | Sparse sources in Time-frequency domain |
| WAIC-UP | Boomless | High | Wavelet | Yes | Monoaxial | 5 | 2 | Interference much larger than intrinsic instrument noise |

*Note*. The Boom column lists the suggested boom length for each algorithm. The streamable column refers to the capability of the algorithm to operate in real-time. The Axis column describes whether the algorithm requires triaxial or monoaxial data to run. The Benchmark Rank columns show the ranking of the algorithms by RMSE.

used in this work represent a highly challenging scenario with more interference sources than magnetometers, broadband interference, and continuous presence of interference throughout the signal duration. While several algorithms did not perform well under these conditions, they may still be suitable for different spacecraft environments. Including these algorithms in the MAGPRIME library provides a pathway for ongoing development and offers valuable resources to the open-source community. Finally, each algorithm has an ideal magnetometer placement within a spacecraft to maximize its effectiveness. For instance, Ness requires two magnetometers on a boom, while UBSS works best when magnetometers are positioned to maximize orthogonality between mixing vectors in its mixing matrix (Candes & Wakin, 2008). An application of MAGPRIME involves determining the optimal magnetometer placements based on a spacecraft's design. However, in our Monte Carlo simulations, the magnetometer locations were fixed and not optimized, which could have influenced the results.

The MAGPRIME library aims to facilitate the collaborative development of interference removal algorithms and simplify the design and integration of spaceflight magnetometers. By establishing two benchmarks, we assessed the effectiveness of MAGPRIME's algorithms using SNR, RMSE, and correlation metrics. These benchmarks reveal that long mechanical booms remain the standard in spaceflight magnetometer design, yet algorithms like UBSS and Ness not only enhance the benefits of a boom but can also reduce its length requirements. The second benchmark highlighted that various algorithms are effective for boomless magnetometer designs, with UBSS demonstrating superior interference reduction capabilities. Future directions for the MAGPRIME library include refining the performance of existing algorithms and incorporating additional interference removal algorithms. Moreover, MAGPRIME also enabled streamlined studies on optimal boom lengths or the number of magnetometers for boomless spacecraft designs. As a community-led initiative, we invite interested individuals to contribute to the ongoing development of MAGPRIME.

## 6. Conclusion

This study introduced MAGPRIME as an innovative, open-source Python library with significant potential to advance in situ space exploration missions. Its extensive suite of magnetic interference removal algorithms, rigorously evaluated through two statistical benchmarks, offers a toolset for scientists and engineers. Benchmark

A underscored the effectiveness of algorithms like UBSS and gradiometry by Ness et al. (1971), which demonstrated superior interference reduction capabilities even over traditional boom-mounted magnetometers. This highlighted the potential to optimize boom length and achieve high fidelity in magnetic field measurements.

Benchmark B explored the performance of MAGPRIME's algorithms in more challenging, boomless magnetometer configuration. The standout performance of UBSS in this benchmark, showing significant interference reduction with median RMSEs significantly lower than unprocessed signals, illustrates its utility in compact, cost-effective spacecraft designs. This finding is particularly relevant for CubeSats and constellation satellites where design and budget considerations are paramount.

MAGPRIME's benchmarks validate its current algorithms and set the stage for further advancements. The library will evolve with the development of new algorithms and the refinement of existing ones. As a community-driven project, MAGPRIME is an new and potentially useful resource in space magnetism research. It supports various phases of spacecraft missions, from design and development to operational data processing, improving the precision of magnetic field measurements.

## Data Availability Statement

All of the codes for the MAGPRIME Library are available at https://doi.org/10.5281/zenodo.11267195. The library contains instructions for installation in the readme file, as well as several tutorial Jupyter notebooks. The Swarm magnetometer data are available from https://swarm-diss.eo.esa.int under MAGx HR in the Level 1B data products folder (Friis-Christensen et al., 2008). The Michibiki QZS-1 Magnetometer data are available at https://sees.tksc.jaxa.jp/fw/dfw/SEES/English/Papers/data/2020/peer_reviewed/01/2020_reviewed_01.shtml (Imajo et al., 2021).

**Acknowledgments**
This research was supported in part through computational resources and services provided by Advanced Research Computing at the University of Michigan, Ann Arbor. This work was partially supported by the NASA HERMES/NEMISIS Grant (80GSFC20C0075), the NASA GDC/NEMISIS Grant (80GSFC23CA042) and a NASA FINESST Fellowship (80NSSC23K1619).

## References

Auster, H. U., Glassmeier, K. H., Magnes, W., Aydogar, O., Baumjohann, W., Constantinescu, D., et al. (2008). The THEMIS fluxgate magnetometer. *Space Science Reviews*, *141*(1), 235–264. https://doi.org/10.1007/s11214-008-9365-9

Boschetti, D., Gervasio, G., & Marziali, I. (2012). Montecarlo approach for magnetic cleanliness evaluation on spacecraft. In *2012 ESA workshop on aerospace EMC* (pp. 1–3). Retrieved from https://ieeexplore.ieee.org/document/6232559

Broadfoot, R. M., Miles, D. M., Holley, W., & Howarth, A. D. (2022). In situ calibration of the Swarm-Echo magnetometers. *Geoscientific Instrumentation, Methods and Data Systems*, *11*(2), 323–333. https://doi.org/10.5194/gi-11-323-2022

Califf, S., Early, D., Grotenhuis, M., Loto'aniu, T. M., & Kronenwetter, J. (2020). Correcting the arcjet thruster disturbance in GOES-16 magnetometer data. *Space Weather*, *18*(1), e2019SW002347. https://doi.org/10.1029/2019SW002347

Candes, E. J., & Wakin, M. B. (2008). An introduction to compressive sampling. *IEEE Signal Processing Magazine*, *25*(2), 21–30. https://doi.org/10.1109/MSP.2007.914731

Carter, D., Freesland, D., Tadikonda, S. K., Kronenwetter, J., Todirita, M., Dahya, M., & Chu, D. (2016). Correcting GOES-R magnetometer data for stray fields. In *2016 ESA workshop on aerospace EMC (aerospace EMC)* (pp. 1–6). IEEE. https://doi.org/10.1109/AeroEMC.2016.7504597

Constantinescu, O. D., Auster, H.-U., Delva, M., Hillenmaier, O., Magnes, W., & Plaschke, F. (2020). Maximum-variance gradiometer technique for removal of spacecraft-generated disturbances from magnetic field data. *Geoscientific Instrumentation, Methods and Data Systems*, *9*(2), 451–469. https://doi.org/10.5194/gi-9-451-2020

Dolginov, S. S., Zhuzgov, L. N., & Seliutin, V. A. (1961). Magnetometric equipment of the third soviet artificial Earth satellite. *ARS Journal*, *31*(9), 1329–1341. https://doi.org/10.2514/8.5776

Finley, M. G., Broadfoot, R. M., Shekhar, S., & Miles, D. M. (2023). Identification and removal of reaction wheel interference from in-situ magnetic field data using multichannel singular spectrum analysis. *Journal of Geophysical Research: Space Physics*, *128*(2), e2022JA031020. https://doi.org/10.1029/2022JA031020

Foster, C. C., & Elkaim, G. H. (2008). Extension of a two-step calibration methodology to include nonorthogonal sensor axes. *IEEE Transactions on Aerospace and Electronic Systems*, *44*(3), 1070–1078. https://doi.org/10.1109/TAES.2008.4655364

Friis-Christensen, E., Lühr, H., Knudsen, D., & Haagmans, R. (2008). Swarm—An Earth observation mission investigating geospace. *Advances in Space Research*, *41*(1), 210–216. https://doi.org/10.1016/j.asr.2006.10.008

Golyandina, N., Korobeynikov, A., & Zhigljavsky, A. (2018). *Singular spectrum analysis with r*. Springer.

Gustetic, J. L., Crusan, J., Rader, S., & Ortega, S. (2015). Outcome-driven open innovation at NASA. *Space Policy*, *34*, 11–17. https://doi.org/10.1016/j.spacepol.2015.06.002

Hoffmann, A. P., & Moldwin, M. B. (2022). Separation of spacecraft noise from geomagnetic field observations through density-based cluster analysis and compressive sensing. *Journal of Geophysical Research: Space Physics*, *127*(9), e2022JA030757. https://doi.org/10.1029/2022JA030757

Hoffmann, A. P., & Moldwin, M. B. (2023). Wavelet-adaptive interference cancellation for underdetermined platforms: Enhancing boomless magnetic field measurements on compact spacecraft. *IEEE Transactions on Aerospace and Electronic Systems*, *59*(6), 1–10. https://doi.org/10.1109/TAES.2023.3315220

Hoffmann, A. P., Moldwin, M. B., Strabel, B. P., & Ojeda, L. V. (2023). Enabling boomless CubeSat magnetic field measurements with the Quad-Mag magnetometer and an improved underdetermined blind source separation algorithm. *Journal of Geophysical Research: Space Physics*, *128*(9), e2023JA031662. https://doi.org/10.1029/2023JA031662

Hyvärinen, A., & Oja, E. (2000). Independent component analysis: Algorithms and applications. *Neural Networks*, *13*(4), 411–430. https://doi.org/10.1016/S0893-6080(00)00026-5

Imajo, S., Nosé, M., Aida, M., Matsumoto, H., Higashio, N., Tokunaga, T., & Matsuoka, A. (2021). Signal and noise separation from satellite magnetic field data through independent component analysis: Prospect of magnetic measurements without boom and noise source information. *Journal of Geophysical Research: Space Physics*, *126*(5), e2020JA028790. https://doi.org/10.1029/2020JA028790

Jo, W., Jin, H., Park, H., Jang, Y., Lee, S., Kim, K.-H., et al. (2023). Korea pathfinder lunar orbiter magnetometer instrument and initial data processing. *Journal of Astronomy and Space Sciences*, *40*(4), 199–215. https://doi.org/10.5140/JASS.2023.40.4.199

Johnson, C. L., Mittelholz, A., Langlais, B., Russell, C. T., Ansan, V., Banfield, D., et al. (2020). Crustal and time-varying magnetic fields at the InSight landing site on Mars. *Nature Geoscience*, *13*(3), 199–204. https://doi.org/10.1038/s41561-020-0537-x

Kilcommons, L. M., Redmon, R. J., & Knipp, D. J. (2017). A new DMSP magnetometer and auroral boundary data set and estimates of field-aligned currents in dynamic auroral boundary coordinates. *Journal of Geophysical Research: Space Physics*, *122*(8), 9068–9079. https://doi.org/10.1002/2016JA023342

Kivelson, M. G., Jia, X., Lee, K. A., Raymond, C. A., Khurana, K. K., Perley, M. O., et al. (2023). The Europa clipper magnetometer. *Space Science Reviews*, *219*(6), 48. https://doi.org/10.1007/s11214-023-00989-5

Lassakeur, A., Underwood, C., Taylor, B., & Duke, R. (2020). Magnetic cleanliness program on CubeSats and nanosatellites for improved attitude stability. *Journal of Aeronautics and Space Technologies*, *13*(1), 25–41. Retrieved from https://jast.hho.msu.edu.tr/index.php/JAST/article/view/387

Lee, J., Jin, H., Kim, K.-H., Park, H., Jo, W., Jang, Y., et al. (2023). Correction of spacecraft magnetic field noise: Initial Korean pathfinder lunar orbiter MAGnetometer observation in solar wind. *Sensors*, *23*(23), 9428. https://doi.org/10.3390/s23239428

Loto'aniu, T. M., Redmon, R. J., Califf, S., Singer, H. J., Rowland, W., Macintyre, S., et al. (2019). The GOES-16 spacecraft science magnetometer. *Space Science Reviews*, *215*(4), 32. https://doi.org/10.1007/s11214-019-0600-3

Ludlam, M., Angelopoulos, V., Taylor, E., Snare, R. C., Means, J. D., Ge, Y. S., et al. (2009). The THEMIS magnetic cleanliness program. In J. L. Burch, & V. Angelopoulos (Eds.), *The THEMIS mission* (pp. 171–184). Springer. https://doi.org/10.1007/978-0-387-89820-9_8

Miles, D. M., Mann, I. R., Ciurzynski, M., Barona, D., Narod, B. B., Bennest, J. R., et al. (2016). A miniature, low-power scientific fluxgate magnetometer: A stepping-stone to cube-satellite constellation missions. *Journal of Geophysical Research: Space Physics*, *121*(12), 11839–11860. https://doi.org/10.1002/2016JA023147

Ness, N. F., Behannon, K. W., Lepping, R. P., & Schatten, K. H. (1971). Use of two magnetometers for magnetic field measurements on a spacecraft. *Journal of Geophysical Research*, *76*(16), 3564–3573. https://doi.org/10.1029/JA076i016p03564

Nikolopoulos, C. D., Baklezos, A. T., & Capsalis, C. N. (2020). On achieving spacecraft level magnetic cleanliness with proper equipment ordinance of DC and ELF magnetic sources. *IEEE Transactions on Electromagnetic Compatibility*, *62*(6), 2714–2724. https://doi.org/10.1109/TEMC.2020.2992682

Park, H. H., Jin, H., Kim, T. Y., Kim, K. H., Lee, H. J., Shin, J. H., et al. (2022). Analysis of the KPLO magnetic cleanliness for the KMAG instrument. *Advances in Space Research*, *69*(2), 1198–1204. https://doi.org/10.1016/j.asr.2021.11.015

Ream, J. B., Weiss, B. P., Oran, R., Raymond, C. A., Polanskey, C. A., Wenkert, D. D., et al. (2021). Magnetic gradiometry using frequency-domain filtering. *Measurement Science and Technology*, *33*(1), 015104. https://doi.org/10.1088/1361-6501/ac2e2e

Sheinker, A., & Moldwin, M. B. (2016). Adaptive interference cancelation using a pair of magnetometers. *IEEE Transactions on Aerospace and Electronic Systems*, *52*(1), 307–318. https://doi.org/10.1109/TAES.2015.150192

Springmann, J. C., & Cutler, J. W. (2012). Attitude-independent magnetometer calibration with time-varying bias. *Journal of Guidance, Control, and Dynamics*, *35*(4), 1080–1088. https://doi.org/10.2514/1.56726

Strabel, B. P., Regoli, L. H., Moldwin, M. B., Ojeda, L. V., Shi, Y., Thoma, J. D., et al. (2022). Quad-Mag board for CubeSat applications. *Geoscientific Instrumentation, Methods and Data Systems*, *11*(2), 375–388. https://doi.org/10.5194/gi-11-375-2022

Vasconcelos, J. F., Elkaim, G., Silvestre, C., Oliveira, P., & Cardeira, B. (2011). Geometric approach to strapdown magnetometer calibration in sensor frame. *IEEE Transactions on Aerospace and Electronic Systems*, *47*(2), 1293–1306. https://doi.org/10.1109/TAES.2011.5751259